

Lawrence Berkeley National Laboratory

LBL Publications

Title

Evaluating impacts of CO2 intrusion into an unconsolidated aquifer: II. Modeling results

Permalink

<https://escholarship.org/uc/item/3276s7fc>

Authors

Zheng, Liange
Qafoku, Nikolla P
Lawter, Amanda
[et al.](#)

Publication Date

2016

DOI

10.1016/j.ijggc.2015.07.001

Peer reviewed

1 Evaluating Impacts of CO₂ Intrusion into an Unconsolidated
2 Aquifer: II. Modeling Results†

3
4 Liange Zheng¹, Nikolla P. Qafoku^{*2}, Amanda Lawter², Guohui Wang², Hongbo Shao²,
5 and Christopher F. Brown²

7 ¹Lawrence Berkeley National Laboratory, Berkeley, CA

8 ²Pacific Northwest National Laboratory (PNNL), Richland, WA

9
10
11 Submitted: December 2014

12 International Journal of Greenhouse Gas Control

13 *Author to whom correspondence should be addressed.

14 Address: Geosciences Group, Earth Systems Science Division, Pacific Northwest
15 National Laboratory, 902 Battelle Boulevard, P.O. Box 999, MSIN: P7-58, Richland, WA 99352

16 E-mail: nik.qafoku@pnl.gov

17 Phone: (509) 371-6089

18 Fax: (509) 371-7249

19 † Electronic Supplementary Information (ESI) available.

20 **ABSTRACT**

21 Large scale deployment of CO₂ geological sequestration requires the assessment of the
22 risks. One of the potential risks is the impact of CO₂ leakage on shallow groundwater overlying
23 the sequestration site. The understanding of the key chemical processes and parameters are
24 critical for building numerical models for risk assessment. Model interpretation of laboratory and
25 field tests is an effective way to enhance such understanding. As part of this investigation,
26 column experiments in which the CO₂ saturated synthetic groundwater flowed through a column
27 packed with materials from the High Plains aquifer, were conducted. Changes in concentrations
28 of several constituents in the column effluent and pH were determined. In this paper, a reactive
29 transport model was developed to describe and interpret the observed concentration changes,
30 attempting to shed light on the chemical reactions and mechanisms and key parameters that
31 control the changes in effluent chemistry. The reactive transport model described fairly well the
32 changes in pH and the concentration changes of Ca, Mg, Ba, Sr, Cs, As and Pb. Calcite
33 dissolution and Ca-driven cation exchange reactions were the major drivers for the concentration
34 changes of Ca, Ba, Sr, and Cs. The pH-driven adsorption/desorption reactions led to a
35 concentration increase of As and Pb. The volume fraction and reactive surface area of calcite,
36 CEC and sorption capacity were key parameters in controlling the magnitude of concentration
37 increase. Model results also showed that Ba, which is an important chemical element released
38 into the aqueous phase during these experiments, may be incorporated into the calcite crystal
39 structure and the dissolution of Ba-bearing calcite could be an alternative pathway to explain the
40 increase in aqueous Ba concentration when sediments are exposed to the CO₂ saturated leaching
41 groundwater.

42 1. INTRODUCTION

43 Geological carbon (C) sequestration is a promising new technology to curb global
44 greenhouse gas emissions. It involves capturing the CO₂ gas emitted from fossil fuel burning
45 power plants, and injecting the captured CO₂ gas into deep saline aquifers or depleted oil and gas
46 reservoirs. Geological C sequestration provides a new approach to combat global warming due to
47 ever rising greenhouse gas emissions by storing it permanently underground. However, a critical
48 question that arises from the proposed geological C sequestration is the potential impacts of the
49 CO₂ injection on the quality of drinking water aquifers overlying C sequestration storage sites.

50 Over the last decade, a number of studies have been undertaken to assess the impacts of
51 potential CO₂ leakage from deep storage reservoirs on the quality of overlying freshwater
52 aquifers (Harvey et al. (2013); Lemieux (2011), and references therein). Numerical modeling has
53 long been used to conduct generic evaluation of the potential groundwater quality change as a
54 result of the hypothetical leakage of CO₂ (Apps et al., 2010; Carroll et al., 2009; Wang and Jaffe,
55 2004; Wilkin and Digiulio, 2010; Zheng et al., 2009), and more importantly to understand the
56 chemical processes that control the CO₂-induced release of metal via model interpretation of
57 laboratory experiments (Kirsch et al., 2014; Viswanathan et al., 2012; Wunsch et al., 2014) and
58 field tests (Trautz et al., 2013b; Zheng et al., 2012).

59 In general these models predicted the release of trace metals such as Pb and As (Apps et
60 al., 2010; Wang and Jaffe, 2004; Zheng et al., 2009), which is largely consistent with the
61 observations from laboratory experiments (Humez et al., 2013; Kirsch et al., 2014; Little and
62 Jackson, 2010; Lu et al., 2010; Smyth et al., 2009; Varadharajan et al., 2013; Viswanathan et al.,
63 2012; Wunsch et al., 2014), although the type of metal being released and the severity of release

64 vary among these experiments. In field tests, however, release of trace metals, especially those
65 of environmental relevance such as As, Pb, Ba, and Cd, has not been observed (Cahill and
66 Jakobsen, 2013; Kharaka et al., 2010; Peter et al., 2012; Spangler et al., 2010; Trautz et al.,
67 2013b; Yang et al., 2013). The difference between the observation of laboratory and field tests in
68 terms of the release of trace metals is probably because the laboratory experiment is too
69 aggressive in leaching out trace metal due to the use of DI water, oxidation, high water/solid
70 ratio and longer reaction time. On the other hand, release of alkali and alkaline earth metals,
71 including Na, K, Ca, Mg, Sr and Ba, were commonly observed both in laboratory and field
72 experiments, although the degree of releases were different. The rise in concentrations of
73 dissolved constituents observed during field tests was typically much less pronounced than in
74 laboratory experiments — field tests show increases about an order of magnitude or less
75 compared to pre-CO₂ levels (20% to 700% in the studies cited above), while orders-of-
76 magnitude increases have been observed in laboratory tests.

77 While the increase in concentration of dissolved constituents raises concerns, a lot of
78 efforts have been invested to understand the controlling chemical processes via model
79 interpretation of laboratory experiments (Viswanathan et al., 2012) and field tests (Zheng et al.,
80 2012). These efforts will facilitate the development of numerical models which will have a
81 better predictability. The chemical processes potentially responsible for the mobilization of trace
82 elements (due to an increase in aqueous carbonate concentration and the decrease of pH include
83 the dissolution of carbonates (Birkholzer et al., 2008; Kharaka et al., 2006b; McGrath et al.,
84 2007), sulfides (Apps et al., 2010; Wang and Jaffe, 2004; Zheng et al., 2009) and iron
85 oxyhydroxide minerals (Kharaka et al., 2006a; Kharaka et al., 2009), as well as surface reactions

86 such as adsorption/desorption and ion exchange (Apps et al., 2010; Kharaka et al., 2006a;
87 Kharaka et al., 2009; Zheng et al., 2009). The release of alkali and alkaline earth metals,
88 including Na, K, Ca, Mg, Sr and Ba, which are most commonly observed both in laboratory and
89 field experiments, is thought to be controlled by the dissolution of calcite and Ca-driven cation
90 exchange reactions (Zheng et al., 2012). The reaction path proposed and kinetic model study
91 conducted by Wilkin and Digiulio (2010) further indicates that the geochemical response of an
92 aquifer to CO₂ leakage is closely related to the aquifer mineralogy. It is thus expected that
93 differences in mineralogy in addition to differences in geology (i.e., aquifer type), and
94 groundwater chemistry at any particular site could lead to different responses to CO₂ leakage.
95 For this reason, experimental laboratory work and field tests coupled with modeling studies are
96 necessary to assess the response of a particular aquifer and evaluate potential changes in
97 groundwater quality and risks related to a CO₂ release.

98 The objective of this study is to determine the geochemical reactions that occur and influence
99 changes in pH and trace metal mobilizations in groundwater aquifers after the intrusion of the
100 CO₂ gas. Batch and column experiments in which materials from the High Plains aquifer were
101 exposed to CO₂ saturated synthetic groundwater (SGW) were conducted to simulate the impact
102 of an accidental release of CO₂ on a shallow aquifer. These experiments are presented in the first
103 paper of this two paper series (Lawter et al., 2015). A reactive transport model was developed to
104 interpret the observed concentration changes in the column effluent water, attempting to shed
105 light on the chemical reactions and key parameters that control the concentration changes of
106 some constituents. Modeling the batch experiment presented in the first paper of this series
107 (Lawter et al., 2015) would help to improve and/or further consolidate the geochemical

108 conceptual model and the reactive transport model, but which have been previously developed
109 based on the batch experiments conducted on other sand-based sediment (Zheng et al., 2015).

110
111 **2. COLUMN EXPERIMENTS**

112 **2.1 Materials and Methods**

113 Modeling was based on column experiments conducted on sediments from the High
114 Plains aquifer in Kansas, obtained from the Drill Core Library at the Kansas Geological Survey.
115 Sediments originated from a single well (CNG), but depths varied from 8 feet to 150 feet. The
116 sediments used in this study were from 58'-60' (CNG 60) and 109'-111' (CNG 110).
117 Characterizations were conducted for these sediment samples to determine chemical
118 composition, crystallization, and surface morphology. Acid extractions conducted on the
119 sediments revealed the sediments contained contaminants of concern for groundwater quality,
120 such as As, Sr, and Pb. The SGW with a chemical composition and pH similar to that of the High
121 Plains aquifer [based on USGS groundwater data for the High Plains aquifer (Becker et al.,
122 2002)], was used in all laboratory experiments and as the influent solution in the models. The
123 recipe used to make SGW is given in Lawter et al. (2015); the composition of the SGW is listed
124 in Table 1.

125 The column experiments are explained in more detail in Lawter et al. (2015), but will be
126 described briefly here. The columns were conducted at room temperature (21 ± 2 °C) and were
127 initially leached with SGW for several days to achieve hydrological equilibrium (i.e., full
128 saturation) and were then leached with CO₂ gas-saturated SGW. CO₂ gas was continuously
129 purged in the influent bottle at a rate of 0.5 mL/min. Stop flow conditions were used to

130 determine the effect of increased fluid residence time on elemental release to observe time-
131 dependent reactions and processes in the columns. Stop flow conditions were applied after the
132 initial leaching with SGW prior to CO₂ injection (time = 70 hours, stopped for 170 hours) then
133 twice more at approximately 250 hours and 350 hours, with the stop flows lasting 122 hours.
134 During the experiment, about one sample per pore volume (PV) was collected, while the effluent
135 samples were collected more frequently after the stop-flow events. The pH was measured
136 continuously online. At the end of the experiments, selected effluent samples were analyzed by
137 both ICP-OES and -MS to determine the aqueous concentrations of major, minor, and trace
138 elements. Column parameters and other related information are listed in Table 2.

139 **2.2 Sediment Characterization: XRD and SEM/EDS**

140 Full results can be found in Qafoku et al. (2013), Shao et al. (2014) and Lawter et al.
141 (2014) but a summary is provided below. Quantitative XRD analyses (QXRD) were conducted
142 for the High Plain aquifer sediments used in this work. The results indicate that quartz and
143 feldspar are the major minerals for the sediments (Qafoku et al., 2013). Small amounts of mica
144 were also detected in the silt fraction of both samples. For the <2mm fraction used in the
145 experiments, CNG 110 contained 1% calcite (the silt and clay fractions contained 35% and 11%
146 calcite, respectively), but no detectable calcite was found in CNG 60. Scanning Electron
147 Microscopy (SEM) and Energy-Dispersive X-ray Spectroscopy (EDS) data shows the presence
148 of Ca bearing phases in CNG 60 (most likely, calcite coatings), which was undetected in the
149 QXRD results (Lawter et al., 2014). These results indicate that the sandy sediments used in this
150 work represent one aquifer type (largely unconsolidated aquifers) overlying potential CO₂
151 sequestration repositories within the continental US.

152

153 3. MODELING

154 3.1 Model setup

155

156 A 1-D reactive transport model was developed to mimic the conditions applied to the
157 column tests. A fixed flow rate is applied to one end of the column and open boundary is used for
158 the other end of column. During stop flow events, the flow rate is adjusted to zero. Chemical
159 reactions considered in the model are aqueous complexation, adsorption/desorption via surface
160 complexation, cation exchange (using the Gaines-Thomas convention) and mineral precipitation/
161 dissolution under kinetic constraints (using published rate laws). The cation exchange reactions
162 are listed in Table 1, with selectivity coefficients from Appelo and Postma (1994) and a CEC of
163 1.55 meq/100g calibrated based on measured breakthrough curve. The surface complexation
164 reactions are listed in Table 2. In the current model, it is assumed that ferrihydrite [as
165 $\text{Fe}(\text{OH})_3(\text{s})$], is the adsorbent. The reaction constants for surface protonation are taken from
166 Dzombak and Morel (1990), and surface complexation reactions of carbonate from Appelo et al.
167 (2002). The model considered quartz, K-feldspar and muscovite as the major aquifer minerals,
168 with a small amount of calcite, magnesite and $\text{Fe}(\text{OH})_3(\text{s})$, based on QXRD results, with a full
169 list of mineralogical composition listed in Table 3. Calcite and magnesite were not detected
170 using QXRD for sample CNG 60; the calcite volume fraction was calibrated based on the
171 measured breakthrough curve of Ca and pH, and that for magnesite was calibrated from the
172 measured breakthrough curve of Mg and pH. In the current model, $\text{Fe}(\text{OH})_3(\text{s})$ was used as the
173 proxy of all possible adsorbents and its amount was calibrated based on the measured
174 breakthrough curve of pH and As. Equilibrium constants for these minerals and other secondary

175 phases allowed to form are given in Table 3. These data were taken from Data0.dat.YMPv4.0, a
176 EQ3/6 (Wolery, 1993) database qualified by the U.S. Department of Energy for the Yucca
177 Mountain.

178 As SGW initially displaces the pore water residing in the column, the measured
179 concentrations for the first effluent water sample actually represents the initial water composition
180 in the column. The model therefore uses first measured concentration of the effluent as the initial
181 concentrations. The concentrations of major cations and anions in the SGW were calculated from
182 the recipe found in Lawter et al. (2014) and those for the trace elements are assigned small
183 values of 10^{-15} . The SGW was pH adjusted to a value of 7.5 prior to the start of the experiment
184 and the concentration of dissolved CO_2 is calculated by assuming equilibrium with atmosphere
185 (CO_2 partial pressure of $10^{-3.4}$ bar), which yields a total concentration of dissolved CO_2 of
186 2.35×10^{-4} M. After the SGW is purged with CO_2 , the pH decreases to 4 and the concentration of
187 dissolved CO_2 is calculated by equilibrating with CO_2 partial pressure of 0.14 bar (2 PSI, see
188 Table 2) which leads to a total dissolved CO_2 concentration of 5.1×10^{-3} M.

189 The simulations were conducted with TOUGHREACT Version 2 (Xu et al., 2011), which
190 implements a general form of rate law for the dissolution and precipitation of solid phases
191 (Lasaga et al., 1994; Steefel and Lasaga, 1994):

$$r = kA \left| 1 - \left(\frac{K}{Q} \right)^{\theta} \right|^{\eta} \quad (1)$$

192

193 where r is the kinetic rate, k is the rate constant ($\text{mol}/\text{m}^2/\text{s}$) which is temperature dependent, A is
194 the reactive surface area per kg water, K is the equilibrium constant for the mineral–water

195 reaction written for the destruction of one mole of mineral, and Q is the reaction quotient. Here,
 196 for simplicity, the exponents θ and η are assumed equal to 1. The reactive surface area, A, is a
 197 function of the mineral specific surface area (e.g., cm²/g mineral) and the volume fraction of the
 198 mineral in the sediment.

199 The rate constant for calcite dissolution is given as a combination of neutral, acid and
 200 carbonate mechanisms (Palandri et al., 2005; Plummer et al., 1979):

201

$$k_{\square} = 1.5 \times 10^{-6} e^{-E_a^{nu}/RT} + 0.5 e^{-E_a^H/RT} a_H + 9.6 \times 10^{-5} e^{-E_a^{CO2}/RT} a_{CO2} \quad (2)$$

202

203 where E_a^{nu} , E_a^H and E_a^{CO2} are activation energies with values of 23.5, 14.4 and 35.4 (kJ/mol),
 204 respectively. The rate constant for the neutral, acid and carbonate mechanisms, are respectively
 205 1.5×10^{-6} (mol/m²/s), 0.5 (mol/m²/s/M) and 9.6×10^{-5} (mol/m²/s/M). a_H is the H⁺ activity and a_{CO2}
 206 is the activity of dissolved CO₂. In the model, the specific surface area of calcite (60 cm²/g) was
 207 calibrated, together with the initial calcite volume fraction, to match the breakthrough of alkaline
 208 earth metals observed for the column test on sample CNG 60. The same specific surface area of
 209 calcite is also used in the base model for sample CNG 110.

210 The rate constant for magnesite dissolution is also given as a combination of neutral, acid
 211 and carbonate mechanisms (Palandri et al., 2005):

212

$$k_{\square} = 4.75 \times 10^{-10} e^{-E_a^{nu}/RT} + 4.16 \times 10^{-7} e^{-E_a^H/RT} a_H + 1.74 \times 10^{-6} e^{-E_a^{CO2}/RT} a_{CO2} \quad (3)$$

213 where E_a^{nu} , E_a^H and $E_a^{CO_2}$ are activation energies with values of 23.5, 14.4 and 62.8 (kJ/mol),
214 respectively. The rate constant for the neutral, acid and carbonate mechanisms, are respectively
215 4.75×10^{-10} (mol/m²/s), 1.46×10^{-7} (mol/m²/s/M) and 1.74×10^{-6} (mol/m²/s/M). In the model, the
216 specific surface area of magnesite (200 cm²/g) was calibrated, together with the initial magnesite
217 volume fraction, to match the breakthrough of Mg and pH observed for the column test on
218 sample CNG 60. We use the same specific surface area of magnesite in the base model for
219 sample CNG 110.

220 Because minerals other than calcite and magnesite have negligible effects on the chemical
221 changes in the column due to the short duration of the experiment, their surface areas and rate
222 constant are taken from Xu et al. (2006) and Zheng et al. (2012) without further calibration. Note
223 that Fe(OH)₃(s) has intangible dissolution over the course of the experiment, which means its
224 dissolution has little effect on the chemical change in the experiment, and as the adsorbent it is
225 important.

226 **3.2. Modeling results**

227 The focus of this paper is the interpretation of concentration changes observed in the
228 CNG 60 column, which shows systematical and well correlated changes in concentration of
229 various elements. The model interpretation of pH, and some alkali and alkaline earth metals
230 including Ca, Mg, Ba, Sr and Cs whose changes have been widely observed in the laboratory and
231 field tests, and As and Pb which are of great environmental concern and less commonly observed
232 in the field and lab tests are specifically targeted. A model for the column test on sample CNG
233 110 was also developed based on that for CNG 60.

234 **3.2.1. Models for the CNG 60 column: The base case**

235 The pH drops immediately following flowing CO₂ saturated SGW through the column,
236 although the extent of drop varies depending on the pH buffering processes. Figure 1 shows the
237 comparison of the measured and simulated pH for the CNG 60 column experiment. In the current
238 model, dissolution of calcite and magnesite are the major reactions that buffer pH, with less pH
239 buffering effect from the surface protonation. The pH buffering by the dissolution of calcite has
240 been well understood and demonstrated (Birkholzer et al., 2008; Carroll et al., 2009; Wang and
241 Jaffe, 2004); the pH buffering by the surface protonation is also well known and has been
242 demonstrated recently in the context of the impact of CO₂ leakage on groundwater (Zheng et al.,
243 2009; Zheng et al., 2012). However, the effect of magnesite dissolution on pH is not widely
244 reported. As demonstrated in Figure 3, removal of magnesite leads to underestimation of pH
245 after around 400 hours. As the CO₂ saturated SGW flushes through the column, calcite
246 dissolution is the primary pH buffer process. After about 400-500 hours, calcite is most likely
247 depleted. Because surface protonation has limited pH buffer capacity, pH keeps decreasing and
248 eventually reaches a level close to the pH of the injected SGW (pH = 4), if additional pH
249 buffering from magnesite dissolution is not considered (Figure 3, “model no magnesite”). This
250 motivates the consideration of magnesite in the base model. Also motivating the inclusion of
251 magnesite in the model is the concentration level of Mg, which will be discussed later (Figure 2).

252 Measured breakthrough curves for Ca, Ba, Sr and Cs show a similar trend — a sharp
253 increase in concentration upon the arrival of CO₂ saturated SGW and then a quick drop. A
254 similar trend has also been observed in a field test conducted in Mississippi (Trautz et al.,
255 2013b), which was interpreted with a model concept that considered the dissolution of minute
256 amount of calcite and the concurrent cation exchange reactions (Trautz et al., 2013b; Zheng et

257 al., 2012). Here we apply the same concept but recalibrate the quantity of calcite and surface area
258 (which affect the dissolution rate of calcite). A volume fraction of 0.045% and a specific surface
259 area of 60 cm²/g are used for calcite, which leads to a decent fit of the measured breakthrough
260 curve of Ca as shown in Figure 1. Calcite is not observed by XRD because the volume fraction is
261 well below the detection limit of 1%, but Ca bearing coating was detected in CNG 60 by
262 SEM/EDS analysis. It is also noteworthy that a volume fraction of calcite below the XRD
263 detection limit is also used in the model for the field test described in Trautz et al. (2013a), where
264 the presence of calcite in the sediments was later confirmed by micro-X ray spectroscopy. The
265 specific surface area of 60 cm²/g for calcite is also higher than that used in Trautz et al. (2013a)
266 (9.8 cm²/g), which is justified considering the difference between the column test with <2 mm
267 sample in this paper and the field test in Trautz et al. (2013b). Because the dissolution rate of
268 calcite is a function of pH and dissolved CO₂ (or CO₂ partial pressure) as shown in Equation (2),
269 the dissolution of calcite is significantly accelerated upon the arrival of CO₂ saturated SGW
270 which is low in pH and high in dissolved CO₂. Such an acceleration of calcite dissolution is the
271 key for a sharp increase in Ca concentration, but the concentration decrease after the peak
272 (Figure 1) is due to the depletion of calcite.

273 The increase in Ca concentration due to calcite dissolution triggers a series of cation
274 exchange reactions. As a result, the concentrations of most alkali and alkaline earth metals show
275 a similar pulse-like shape in the breakthrough curves, e.g., Sr, Ba (Figure 1) and Cs (Figure 2).
276 The model reasonably follows the measured breakthrough curves of Sr and Cs, but
277 underestimates the measured data of Ba although qualitatively the model results and data for Ba
278 match. The quantitative mismatch between model results and data for Ba could be eased if

279 another Ba release mechanism is considered, which will be discussed later in this paper. In the
280 current model, Mn is controlled only by cation exchange reaction. Model results match the first
281 peak in the Mn breakthrough curve but fail to catch the stepwise increase in the Mn
282 concentration in the effluent (Figure 2). The fact that Mn concentration keeps increasing
283 indicates there is dissolution of Mn bearing minerals. However, no Mn bearing minerals were
284 detected in mineral characterization; they might be of too small quantity to be identified.
285 Interestingly the breakthrough curve of Si shows a pattern (Figure 2) similar to Ca, Cs, Sr and
286 Ba, except Si has a more pronounced peak after the second and third stop-flow events. The
287 similarity between Si and Ca breakthrough had also been observed in a field test in
288 Mississippi (Pugh et al., 2013). Because Si bearing minerals are unlikely to dissolve as quickly
289 as calcite, and based on findings previously presented in the literature (Pugh et al., 2013), we
290 included adsorption/desorption reactions for Si in the model (see Table 4) and, as a result, a
291 qualitative match between model and experimental data was achieved for Si (Figure 2).

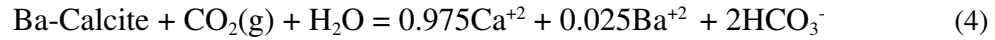
292 The SGW contains a fairly high concentration of Na which largely determines the
293 concentration of Na in the effluent. However, cation exchange with Ca can also cause small
294 pulses in the breakthrough curve of Na, as shown in Figure 2. In addition, the SGW contains
295 about 1.57×10^4 mg/L Mg. Without an additional source of Mg from magnesite, as shown by the
296 “model no magnesite” in Figure 3, cation exchange makes the simulated Mg concentration after
297 the first peak fairly lower than that of measured data. The dissolution of magnesite in the base
298 model improves the fit between measured and simulated Mg concentration. Increasing the
299 dissolution rate of magnesite could raise the concentration level of Mg after the first peak and
300 improve the fit. However, this will drive the pH higher and decrease the fit between measured

301 and simulated pH. If dolomite instead of magnesite is used, model results for Mg are similar, but
302 the fit between measured and simulated pH and Ca become slightly worse.

303 Generic modeling works (Apps et al., 2010; Zheng et al., 2009) and models for the field
304 test (Zheng et al., 2012) have shown that desorption due to pH drop could be the main process
305 that controls the release of trace elements such as As and Pb in response to the CO₂ leakage in
306 groundwater. The close match between the measured and simulated breakthrough curve of As
307 (Figure 1) in this paper seems to support this concept. The surface complexation reactions for As
308 are listed in Table 2; the amount of the adsorbent, which is assumed to be Fe(OH)₃(s) is
309 calibrated. Note that here we use the adsorption/desorption of As from Fe(OH)₃(s) as a proxy of
310 all possible adsorption/desorption reactions including those that could occur on the surface of
311 clay minerals. The fit of measured Pb concentration with model results (Figure 1) is less
312 desirable, but the model catches the concentration changes fairly well after the third stop-flow
313 event.

314 *3.2.2. An alternative model with Ba impurity in calcite*

315 Because most sediments contain some clay and subsequently cation exchange reaction is
316 ubiquitous, the dissolution of calcite and the concurrent Ca-driven cation exchange have been
317 used so far to explain the change of Ba concentration. Another possibility that could not be ruled
318 out is that Ba could be present in calcite as an impurity so that Ba is released concomitantly with
319 Ca as calcite dissolves. This concept has been used by Lu et al. (2010) to interpret the release of
320 metals upon CO₂ intrusion in groundwater in their laboratory experiment. This concept was also
321 tested here by modeling the dissolution of calcite containing 2.5 mol % Ba impurity as shown by
322 the following reaction.



323

324 The equilibrium constant for reaction (4) was calculated by assuming an ideal solid solution
325 between calcite and witherite. This seems to result in a better fit for Ba concentration compared
326 to the base case (Figure 4), suggesting that this is a plausible process for the release of Ba.

327 *3.2.3. Models for the CNG 110 column: The base model*

328 Based on the model for sample CNG 60 and correcting the amount of minerals according
329 to the experimental measurement, a model was created to describe the data collected from the
330 column test conducted with sample CNG 110. CNG 110 differs significantly in the content of
331 calcite with CNG 60. Differences in other major minerals such as quartz and feldspar in sample
332 CNG 110 in comparison with CNG 60 most likely have only negligible effects on elemental
333 concentration changes considering the short duration of the test.

334 Like the model for sediment CNG 60 model, the model for sediment CNG 110 catches
335 the measured breakthrough curve of pH, but the modeling curve starts to deviate after 400 hours
336 of experimental time (Figure 1). The fact that simulated pH remains at the same level before and
337 after 400 hours indicates that calcite has not been depleted. Model results for CNG 60 shows it
338 takes 400-500 hours to run out of calcite at a volume fraction of 0.045%, so it is not possible to
339 deplete 1% calcite in 400 hours.

340 Upon the arrival of CO₂ saturated SGW, the dissolution of calcite leads to a quick
341 increase of Ca concentration and maintains a relatively high level thereafter. On the contrary,
342 measured data shows a slow increase and does not reach the high concentration level shown by
343 model results (Figure 1).

344 In the current model concept, because cation exchange occurs concurrently with calcite
345 dissolution, Sr typically follows the change of Ca, as illustrated by the model and data for the
346 column test of CNG 60. However, in contrast with the slow rising and then somewhat stabilized
347 concentration of Ca, the Sr in the CNG 110 column shows a pulse-like trend. Model results for
348 Sr show a slow rising in concentration and a slow decrease due to the depletion of exchangeable
349 Sr, failing to match the column breakthrough curve for Sr (Figure 1). Similar phenomenon is
350 observed for Ba (Figure 1). The measured Ba breakthrough curve shows sharp pulse-like
351 behavior, in contrast to the slow rising and falling shown by model results.

352 The concept of calcite dissolution and accompanied cation exchange has been used
353 successfully to interpret field tests in Montana (Zheng et al., 2012) and Mississippi (Trautz et al.,
354 2013b). It has also been proved a valid concept for modeling the column test conducted with
355 sediment CNG 60. By varying the amount and dissolution rate of calcite, and CEC, reasonable fit
356 between measured data and model results can be achieved. However, such concept failed to
357 explain the observation in the column test with CNG110. Looking at Figure 1, the dilemma is the
358 mismatch between the Ca breakthrough curve and those for Ba and Sr. Lowering the dissolution
359 rate of calcite could improve the match between measured and simulated Ca concentrations, but
360 would further deteriorate the match between measured and simulated Ba. To match the pulse-like
361 behavior in the breakthrough curve of Ba and Sr, calcite needs to be depleted shortly after the
362 arrival of CO₂-charged SGW, but with 1% calcite present in the sediment, depletion is
363 implausible.

364 The CNG 60 model explains the concentration changes in As and Pb by desorption
365 caused by the drop of pH, but the CNG110 model fails to match the observed data for As and Pb.

366 As the pH in the CNG 110 column test decreases less than that in the test on CNG 60, there is
367 less desorption and therefore As and Pb are lower as shown by the model for CNG 110, although
368 it departs from measured data (Figure 1).

369 ***3.2.4. An alternative model for CNG 110 with higher CEC***

370 The CEC is a key parameter that affects the Ba and Sr solid and liquid phase
371 concentrations. In the base model for CNG 110, a CEC of 1.55 meq/100 g was used which was
372 also used for the model for CNG 60. However, as the clay content in CNG 110 is different, the
373 CEC varies as well. In a sensitivity run, the CEC was increased to 8 meq/100 g, hoping to
374 improve the match between model and measured data. Higher CEC leads to higher concentration
375 after the initial rising, but still fails to make the simulated initial peak closer to the measured data
376 for Ba and Sr (Figure 5).

377 The model for CNG 60 shows that inclusion of Ba impurity in calcite leads to a better fit
378 of measured data of Ba. This was also applied to the model for CNG 110, with 1 mol% Ba
379 included in calcite. The continuous dissolution of calcite results in a sustainable increase in Ba
380 concentration, which deviates significantly from the measured experimental data.

381 **4. DISCUSSION**

382 **4.1. About the initial amount of calcite**

383 In the column test, pH decreases upon the arrival of CO₂-saturated SGW at the outlet, and
384 the Ca concentration soars up quickly and then decreases after reaching a peak concentration.
385 The temporal profiles for the concentration of other alkali and alkaline earth metals such as Sr
386 and Ba in the effluent follow almost precisely the pattern of Ca. Similar patterns of temporal

387 concentration changes have also been observed in a field test conducted in Mississippi (Trautz et
388 al., 2013b). In this test, groundwater from a confined hydrostratigraphic interval was pumped and
389 carbonated above ground, then re-injected into the same interval (in a dipole, closed loop system)
390 of an aquifer at approximately 50 m deep. Injection of carbonated groundwater at this site lasted
391 for around 5 months, preceded by an extensive monitoring period of background conditions and
392 followed by a post-injection monitoring period of around 10 months. Four monitoring wells were
393 emplaced downstream of the injection well. The concentration changes of alkali and alkaline
394 earth metals in the nearest monitoring well shows exactly the same pulse-like shape as we
395 observed in the column tests presented in this paper. To mimic the Ca concentration profile at the
396 Mississippi field test with reactive transport model, a small amount of calcite (~0.006–0.009%),
397 an amount that is enough to create the concentration peak but lead to depletion of calcite after the
398 arrival of CO₂-charged water, has to be used in the model. The concentration change of the rest
399 of the alkali and alkaline earth metals then can be interpreted as Ca-driven cation exchange
400 reaction. However, because calcite were not detected using XRD, doubt on such model
401 interpretation had been raised when the model was first published (Trautz et al., 2013b), despite
402 the amount of calcite used in the model being much lower than the detection limit of XRD. A
403 later laboratory study with the same sediment (Varadharajan et al., 2013) found calcite using
404 micro-X ray spectroscopy, which confirmed the validity of considering a small amount of calcite
405 in the model. Intuitively, we applied the same model concept to interpret the breakthrough curve
406 of Ca, Sr, Cs and Ba for the column test conducted with sample CNG 60, and found a good
407 match between model and experimental data. We therefore conclude that a small amount of
408 calcite does exist in sample CNG 60 as indicated by the SEM/EDS results and despite not being
409 detected by XRD.

410 **4.2. About the impurity of trace metals in calcite**

411 It is not uncommon for calcite to contain metal impurities. Some researchers (Kirsch et
412 al., 2014; Lu et al., 2010; Wunsch et al., 2014) thus proposed the dissolution of calcite with
413 impurities to explain the concurrent rise in concentrations of Ca and other metals. In this paper,
414 we first used the dissolution of calcite and Ca-driven cation exchange to explain the
415 breakthrough curve of Ba, and then tried to use the dissolution of calcite with Ba impurity
416 (Section 3.2.2) to match the data. The former model catches the initial and final concentration of
417 Ba and the latter model catches the peak better. In another study Zheng et al. (2014), we tested
418 both these concepts (or models), and the concept of calcite dissolution with Ba impurity did a
419 less desirable job to match the Ba release from a batch experiment (Varadharajan et al., 2013).
420 These two concepts have the same the reaction kinetics that is controlled by the calcite
421 dissolution rate. The difference between these two concepts is that in the first concept, cations
422 interfere with each other due to competition on exchangeable sites and are constrained by CEC,
423 whereas in the second concept, cations are more independent of each other and are only
424 constrained by the fraction of impurity in the calcite. The conclusion is that both concepts are
425 plausible and a model for a column (or batch) test cannot delineate which one is at play.

426 **4.3. Constraining relevant chemical parameters for large scale model**

427 In the context of assessing the risk of CO₂ leakage on groundwater, reactive transport
428 models are indispensable tools. The predictability of a reactive transport model is dictated by the
429 chemical reactions considered in the model and key parameters for these reactions. Column tests
430 with the sediment from the target aquifer and the interpretive reactive transport model for the
431 column will play a key role in raising our confidence for the large scale reactive transport

432 models. First, a column test is a screening tool to determine which elements could be released by
433 the leakage of CO₂. Batch experiments can be used for such purpose as well, but tend to be too
434 aggressive because of the large water-to-solid ratio and long residence time for water-rock
435 interaction. For example, batch experiments (Varadharajan et al., 2013) were conducted for the
436 sediments from an aquifer where a field test was conducted (Trautz et al., 2013); some elements
437 in the EPA primary groundwater regulation list, such as As, Pb, showed significant increases in
438 the batch experiment, but were not even detected in the field test(Pugh et al., 2013). Because
439 column tests are typically conducted at water-to-solid ratio close to field conditions and take into
440 account the interaction between transport processes and chemical reactions, it is a better proxy to
441 the field condition and therefore a better tool than batch experiments to determine which
442 elements are going to be released. Second, interpretation of column tests with reactive transport
443 models helps to delineate the controlling chemical reactions and calibrate the key parameters.
444 For example, in this paper, a close match between the model and column data for Sr clearly
445 indicates that Ca-driven cation exchange is the reaction that controls the release of Sr, and the
446 reactive surface area of calcite and CEC are the key parameters which can be well constrained
447 from the Ca and Sr breakthrough curves. Matching the As and Pb data with model results
448 confirms the control of adsorption/desorption on the release of As and Pb and can be used to
449 calibrate the amount and surface area of adsorbents.

450 5. CONCLUSIONS

451 To assess the long term risk of CO₂ geological sequestration, numerical models have to
452 be employed to evaluate the potential impact of the CO₂ leakage on shallow groundwater
453 overlying the sequestration site. The understanding of the key chemical processes and parameters

454 are critical for the predictability of numerical models. Model interpretation of laboratory and field
455 tests was an effective way to enhance such understanding. Column experiments in which CO₂
456 saturated SGW flows through a column packed with material from High Plains aquifer were
457 conducted and concentrations of several chemical constituents in the effluent water were
458 determined. In this paper, reactive transport model was developed to interpret the observed
459 concentration changes, attempting to shed light on the chemical reactions and key parameters
460 that control the concentration changes of these constituents.

461 The column test conducted with sediment CNG 60 shows systematical and well
462 correlated changes in concentration of various elements. A reactive transport model can match
463 the concentration changes of pH, Ca, Mg, Ba, Sr, Cs, As and Pb fairly well. Calcite dissolution
464 and Ca-driven cation exchange reactions are the major drivers for the concentration changes of
465 Ca, Ba, Sr, and Cs, which is consistent with the findings revealed by models developed with data
466 generated from other sites (Trautz et al., 2013b; Zheng et al., 2012). The pH-driven
467 adsorption/desorption reactions are the reason for concentration increases of As and Pb. The
468 volume fraction and reactive surface area of calcite, CEC and sorption capacity are key
469 parameters in determining the magnitude of concentration increase. Model results also show that
470 the dissolution of calcite with Ba impurity could be an alternative explanation of the increase in
471 Ba concentration. The model interpretation of column test clearly showed that understanding the
472 metal-sediment association and key parameters are critical for the predictability of numerical
473 models.

474 The model for sample CNG 60 was corrected for the amount of minerals (mainly calcite)
475 based on the measurement for sample CNG 110, to interpret the column test results for the

476 sample CNG 110. Although the model follows well the experimental pH data, it fails to explain
477 the concentration changes of the rest of the constituents. The poor correlation between the
478 concentration of Ca, Ba and Sr, and the erratic concentration of Ca are probably the reasons for
479 the mismatch between data and model. Pb and As data are also quite scattered so that it is hard
480 to draw a clear trend and subsequently to interpret them with a model. While re-examination of
481 the column test for sample CNG 110 and the conceptual geochemical modeling might be helpful
482 for better understanding of the observations from column test for sample CNG 110, it illustrates
483 the challenge we are facing when modeling the intriguing interactions between transport and
484 chemical reactions involved in the test.

485 **ACKNOWLEDGEMENTS**

486 Funding for this research was provided by the National Risk Assessment Partnership
487 (NRAP) in the U.S. DOE Office of Fossil Energy under DOE contract number DE AC05
488 76RL01830. XRD and SEM analysis were performed in the Environmental Molecular Sciences
489 Laboratory (EMSL), a national scientific user facility sponsored by the Department of Energy's
490 Office of Biological and Environmental Research and located at PNNL. PNNL is operated by
491 Battelle for the U.S. DOE under Contract DE-AC06-76RLO 1830. Samples were obtained from
492 the Kansas Geological Survey at Kansas University.

493

494 **FIGURE CAPTIONS**

495

496 **Table 1.** Cation exchange reactions and selectivity coefficients, using the Gaines-
497 Thomas convention (Appelo and Postma, 1994).

498

499 **Table 2.** Surface complexation reactions and surface complexation constants (logK)
500 on ferrihydrite (Dzomback and Morel, 1990; Appelo et al., 2002; Jordan et al., 2007).

501

502

503 **Table 3.** Equilibrium constants (logK) and initial volume fraction of minerals in the
504 sediment (on a dry basis). LogK are for reactions that are written with the primary species
505 listed in the first column of Table 2.

506

507 **FIGURE CAPTIONS**

508 **Figure 1.** Simulated and observed breakthrough curves of pH, Ca, Sr, Ba, As, Pb, Na and Cs for
509 the column test of sample CNG60 (red) and CNG 110 (black). Cs and Na are not included
510 for CNG 110.

511 **Figure 2.** Simulated and observed breakthrough curves of Si, Mn, Na and Cs for the column
512 test of sample CNG60.

513 **Figure 3.** Simulated and observed breakthrough curves of pH and Mg with and without
514 magnesite included in the model for the column test of sample CNG60.

515
516 **Figure 4.** Observed breakthrough curves of Ba for the column test of sample CNG 60 (both
517 graphs) and CNG 110 (right graph), and simulated results in the base model and a model
518 with Ba impurity in calcite.

519 **Figure 5.** Observed breakthrough curves of Ba and Sr for the column test of sample CNG110
520 and simulated results in the base model and a model with higher CEC value.

521
522

523

524 REFERENCES

525

526 Appelo, C. A. J., and Postma, D. (1994). "Geochemistry, groundwater and pollution,"
527 A. A. Balkema, Rotterdam.

528 Appelo, C. A. J., Van der Weiden, M. J. J., Tournassat, C., and Charlet, L. (2002).
529 Surface complexation of ferrous iron and carbonate on ferrihydrite and the
530 mobilization of arsenic. *Environmental Science & Technology* **36**, 3096-3103.

531 Apps, J. A., Zheng, L., Zhang, Y., Xu, T., and Birkholzer, J. T. (2010). Evaluation of
532 potential changes in groundwater quality in response to CO₂ leakage from
533 deep geologic storage. *Transport Porous Med.* **82**, 215-246.

534 Becker, M. F., Bruce, B. W., Pope, L. M., and Andrews, W. J. (2002). "Ground-Water
535 Quality in the Central High Plains Aquifer, Colorado, Kansas, New Mexico,
536 Oklahoma, and Texas, 1999." U.S. Geological Survey.

537 Birkholzer, J. T., Apps, J., Zheng, L., Zhang, Y., Xu, T., and Tsang, C.-F. (2008).
538 "Research project on CO₂ geological storage and groundwater resources,
539 quality effects caused by CO₂ intrusion into shallow groundwater, Technical
540 Report." Earth Sciences Division, Lawrence Berkeley National Laboratory,
541 Berkeley, CA.

542 Cahill, A. G., and Jakobsen, R. (2013). Hydro-geochemical impact of CO₂ leakage
543 from geological storage on shallow potable aquifers: A field scale pilot
544 experiment. *International Journal of Greenhouse Gas Control* **19**, 678-688.

545 Carroll, S., Hao, Y., and Aines, R. (2009). Geochemical detection of carbon dioxide in
546 dilute aquifers. *Geochem. Trans.* **10**,
547 <http://www.geochemicaltransactions.com/content/10/1/4>.

548 Dzombak, D. A., and Morel, F. M. M. (1990). "Surface Complexation Modeling:
549 Hydrous Ferric Oxide," Wiley-Interscience, New York.

550 Harvey, O. R., Qafoku, N. P., Cantrell, K. J., Lee, G., Amonette, G. E., and Brown, C. F.
551 (2013). Geochemical Implications of Gas Leakage associated with Geologic
552 CO₂ Storage-A Qualitative Review. *Environ. Sci. Technol.* **47**, 23-26.

553 Humez, P., Lagneau, V., Lions, J., and Negrel, P. (2013). Assessing the potential
554 consequences of CO₂ leakage to freshwater resources: A batch-reaction
555 experiment towards an isotopic tracing tool. *Applied Geochemistry* **30**, 178-
556 190.

557 Jordan, N., Marmier, N., Lomenech, C., Giffaut, E., and Ehrhardt, J.-J. (2007). Sorption
558 of silicates on goethite, hematite, and magnetite: Experiments and modelling.
559 *Journal of Colloid and Interface Science* **312**, 224-229.

560 Kharaka, Y. K., Cole, D. R., Hovorka, S. D., Gunter, W. D., Knauss, K. G., and Freifeld,
561 B. M. (2006a). Gas-water-rock interactions in Frio Formation following CO₂
562 injection: Implications for the storage of greenhouse gases in sedimentary
563 basins. *Geology* **34**, 577-580.

564 Kharaka, Y. K., Cole, D. R., Thordsen, J. J., Kakouros, E., and Nance, H. S. (2006b).
565 Gas-water-rock interactions in sedimentary basins: CO₂ sequestration in the
566 Frio Formation, Texas, USA. *Journal of Geochemical Exploration* **89**, 183-186.

567 Kharaka, Y. K., Thordsen, J. J., Kakouros, E., Ambats, G., Herkelrather, W. N., Beers,
568 S. R., Birkholzer, J. T., Apps, J. A., Spycher, N. F., Zheng, L., Trautz, R. C.,
569 Rauch, H. W., and Gullickson, K. S. (2010). Changes in the chemistry of
570 shallow groundwater related to the 2008 injection of CO₂ at the ZERT field
571 site, Bozeman, Montana. *Environ. Earth Sci.* **60**, 273-284.

572 Kharaka, Y. K., Thordsen, T. T., Hovorka, S. D., Nance, S., Cole, D. R., Phelps, T. J.,
573 and Knauss, K. G. (2009). Potential environmental issues of CO₂ storage in
574 deep saline aquifers: Geochemical results from the Frio-I Brine Pilot test,
575 Texas, USA. *Applied Geochemistry* **24**, 1106-1112.

576 Kirsch, K., Navarre-Sitchler, A. K., Wunsch, A., and McCray, J. E. (2014). Metal
577 release from sandstones under experimentally and numerically simulated CO₂
578 leakage conditions. *Environmental Science & Technology* **48**, 1436-1442.

579 Lasaga, A. C., Soler, J. M., Ganor, J., Burch, T. E., and Nagy, K. L. (1994). CHEMICAL-
580 WEATHERING RATE LAWS AND GLOBAL GEOCHEMICAL CYCLES. *Geochimica
581 Et Cosmochimica Acta* **58**, 2361-2386.

582 Lawter, A., Qafoku, N., Wang, G., Shao, H., and Brown, C. (2014). Evaluating and
583 Predicting Impacts of CO₂ Intrusion into an Unconsolidated Aquifer: 1.
584 Experimental Data. *submitted*.

585 Lemieux, J.-M. (2011). The potential impact of underground geological storage of
586 carbon dioxide in deep saline aquifers on shallow groundwater resources.
587 *Hydrogeology Journal* **19**, 757-778.

588 Little, M. G., and Jackson, R. B. (2010). Potential Impacts of Leakage from Deep CO₂
589 Geosequestration on Overlying Freshwater Aquifers. *Environ. Sci. Technol.*
590 **44**, 9225-9232.

591 Lu, J., Partin, J. W., Hovorka, S. D., and Wong, C. (2010). Potential risks to freshwater
592 resources as a result of leakage from CO₂ geological storage: a batch-reaction
593 experiment. *Environ. Earth Sci.* **60**, 335-348.

594 McGrath, A. E., Upson, G. L., and Caldwell, M. D. (2007). Evaluation and mitigation
595 of landfill gas impacts on cadmium leaching from native soils. *Ground Water
596 Monitoring and Remediation* **27**, 99-109.

597 Palandri, J. L., Rosenbauer, R. J., and Kharaka, Y. K. (2005). Ferric iron in sediments
598 as a novel CO₂ mineral trap: CO₂-SO₂ reaction with hematite,. *Applied
599 Geochemistry* **20**, 2038-2048.

600 Peter, A., Lamert, H., Beyer, M., Hornbruch, G., Heinrich, B., Schulz, A., Geistlinger,
601 H., Schreiber, B., Dietrich, P., Werban, U., Vogt, C., Richnow, H. H.,
602 Grossmann, J., and Dahmke, A. (2012). Investigation of the geochemical
603 impact of CO₂ on shallow groundwater: design and implementation of a CO₂
604 injection test in Northeast Germany. *Environmental Earth Sciences* **67**, 335-
605 349.

606 Plummer, L., Parkhurst, D., and Wigley, T. (1979). Critical review of the kinetics of
607 calcite dissolution and precipitation. *Chemical Modeling in Aqueous Systems*
608 **93**, 537-573.

609 Pugh, J. D., Varadharajan, C., Zheng, L., Bianchi, M., Nico, P. S., Spycher, N., Newell,
610 D. L., Esposito, R. A., Wu, Y. X., Dafflon, B., Hubbard, S. S., Birkholzer, J., and
611 Trautz, R. (2013). "Potential impact of carbon dioxide on potable
612 groundwater: a controlled release experiment." EPRI.

613 Qafoku, N., Brown, C., Wang, G., Sullivan, E., Lawter, A., Harvey, O., and Bowden, M.
614 (2013). "Geochemical Impacts of Leaking CO₂ from Subsurface Storage
615 Reservoirs to Unconfined and Confined Aquifers," Rep. No. PNNL-22420.
616 Pacific Northwest National Laboratory.

617 Shao, H., Qafoku, N., Lawter, A., Bowden, M., and Brown, C. (2014). Geochemical
618 Impacts of Leaking CO₂ from Subsurface Storage Reservoirs on the
619 Mobilization of Metals from Sediments. *submitted*.

620 Smyth, R. C., Hovorka, S. D., Lu, J., Romanak, K. D., Partin, J. W., Wong, C., and
621 Yang, C. (2009). Assessing risk to fresh water resources from long term CO₂
622 injection-laboratory and field studies. *Energy Procedia* **1**, 1957-1964.

623 Spangler, L. H., Dobeck, L. M., Repasky, K. S., Nehrir, A. R., Humphries, S. D., Barr, J.
624 L., Keith, C. J., Shaw, J. A., Rouse, J. H., Cunningham, A. B., Benson, S. M.,
625 Oldenburg, C. M., Lewicki, J. L., Wells, A. W., Diehl, J. R., Strazisar, B. R.,
626 Fessenden, J. E., Rahn, T. A., Amonette, J. E., Barr, J. L., Pickles, W. L.,
627 Jacobson, J. D., Silver, E. A., Male, E. J., Rauch, H. W., Gullickson, K. S., Trautz,
628 R., Kharaka, Y., Birkholzer, J., and Wielopolski, L. (2010). A shallow subsurface
629 controlled release facility in Bozeman, Montana, USA, for testing near surface
630 CO₂ detection techniques and transport models. *Environmental Earth*
631 *Sciences* **60**, 227-239.

632 Steefel, C. I., and Lasaga, A. C. (1994). A COUPLED MODEL FOR TRANSPORT OF
633 MULTIPLE CHEMICAL-SPECIES AND KINETIC PRECIPITATION DISSOLUTION
634 REACTIONS WITH APPLICATION TO REACTIVE FLOW IN SINGLE-PHASE
635 HYDROTHERMAL SYSTEMS. *American Journal of Science* **294**, 529-592.

636 Trautz, R. C., Pugh, J. D., Varadharajan, C., Zheng, L., Bianchi, M., Nico, P. S.,
637 Spycher, N. F., Newell, D. L., Esposito, R. A., Wu, Y., Dafflon, B., Hubbard, S.
638 S., and Birkholzer, J. T. (2013a). Effect of Dissolved CO₂ on a Shallow
639 Groundwater System: A Controlled Release Field Experiment. *Environmental*
640 *Science & Technology* **47**, 298-305.

641 Trautz, R. C., Pugh, J. D., Varadharajan, C., Zheng, L. G., Bianchi, M., Nico, P. S.,
642 Spycher, N. F., Newell, D. L., Esposito, R. A., Wu, Y. X., Dafflon, B., Hubbard, S.
643 S., and Birkholzer, J. T. (2013b). Effect of Dissolved CO₂ on a Shallow
644 Groundwater System: A Controlled Release Field Experiment. *Environmental*
645 *Science & Technology* **47**, 298-305.

646 Varadharajan, C., Tinnacher, R. M., Pugh, J. D., Trautz, R. C., Zheng, L. G., Spycher,
647 N. F., Birkholzer, J. T., Castillo-Michel, H., Esposito, R. A., and Nico, P. S.
648 (2013). A laboratory study of the initial effects of dissolved carbon dioxide
649 (CO₂) on metal release from shallow sediments. *International Journal of*
650 *Greenhouse Gas Control* **19**, 183-211.

651 Viswanathan, H., Dai, Z. X., Lopano, C., Keating, E., Hakala, J. A., Scheckel, K. G.,
652 Zheng, L. G., Guthrie, G. D., and Pawar, R. (2012). Developing a robust
653 geochemical and reactive transport model to evaluate possible sources of
654 arsenic at the CO₂ sequestration natural analog site in Chimayo, New Mexico.
655 *International Journal of Greenhouse Gas Control* **10**, 199-214.

656 Wang, S., and Jaffe, P. R. (2004). Dissolution of a mineral phase in potable aquifers
657 due to CO₂ releases from deep formations; effect of dissolution kinetics.
658 *Energy Convers. manage.* **45**, 2833-2848.

659 Wilkin, R. T., and Digiulio, D. C. (2010). Geochemical Impacts to Groundwater from
660 Geologic Carbon Sequestration: Controls on pH and Inorganic Carbon
661 Concentrations from Reaction Path and Kinetic Modeling. *Environmental*
662 *Science & Technology* **44**, 4821-4827.

663 Wolery, T. J. (1993). EQ3/6. pp. A software package for geochemical modelling of
664 aqueous systems, Lawrence Livermore National Laboratory.

665 Wunsch, A., Navarre-Sitchler, A. K., Moore, J., and McCray, J. E. (2014). Metal release
666 from limestones at high partial-pressures of CO₂. *Chemical Geology* **363**, 40-
667 55.

668 Xu, T. F., Sonnenthal, E., Spycher, N., and Pruess, K. (2006). TOUGHREACT - A
669 simulation program for non-isothermal multiphase reactive geochemical

670 transport in variably saturated geologic media: Applications to geothermal
671 injectivity and CO₂ geological sequestration. *Computers & Geosciences* **32**,
672 145-165.

673 Xu, T. F., Spycher, N., Sonnenthal, E., Zhang, G. X., Zheng, L. E., and Pruess, K.
674 (2011). TOUGHREACT Version 2.0: A simulator for subsurface reactive
675 transport under non-isothermal multiphase flow conditions. *Computers &*
676 *Geosciences* **37**, 763-774.

677 Yang, C. B., Mickler, P. J., Reedy, R., Scanlon, B. R., Romanak, K. D., Nicot, J. P.,
678 Hovorka, S. D., Trevino, R. H., and Larson, T. (2013). Single-well push-pull test
679 for assessing potential impacts of CO₂ leakage on groundwater quality in a
680 shallow Gulf Coast aquifer in Cranfield, Mississippi. *International Journal of*
681 *Greenhouse Gas Control* **18**, 375-387.

682 Zheng, L., Apps, J. A., Zhang, Y., Xu, T., and Birkholzer, J. T. (2009). On mobilization
683 of lead and arsenic in groundwater in response to CO₂ leakage from deep
684 geological storage. *Chemical Geology* **268**, 281-297.

685 Zheng, L., Spycher, N., Varadharajan, C., Tinnacher, R. M., Pugh, J. D., Bianchi, M.,
686 J.T., B., Nico, P. S., and Trautz, R. (2014). On the Mobilization of Metals by
687 CO₂ Leakage into Shallow Aquifers: Exploring Release Mechanisms by
688 Modeling Field and Laboratory Experiments. *Greenhouse Gases-Science and*
689 *Technology* **In review**.

690 Zheng, L. G., Apps, J. A., Spycher, N., Birkholzer, J. T., Kharaka, Y. K., Thordsen, J.,
691 Beers, S. R., Herkelrath, W. N., Kakouros, E., and Trautz, R. C. (2012).
692 Geochemical modeling of changes in shallow groundwater chemistry
693 observed during the MSU-ZERT CO₂ injection experiment. *International*
694 *Journal of Greenhouse Gas Control* **7**, 202-217.

695